Angewandte Chemie
Eine Zeitschrift der Gesellschaft Deutscher Chemiker

Supporting Information

Access to Heteroleptic Fluorido-Cyanido Complexes with a Large Magnetic Anisotropy by Fluoride Abstraction

Jun-Liang Liu, Kasper S. Pedersen, Samuel M. Greer, Itziar Oyarzabal, Abhishake Mondal, Stephen Hill, Fabrice Wilhelm, Andrei Rogalev, Alain Tressaud, Etienne Durand, Jeffrey R. Long, and Rodolphe Clérac**

anie_201914934_sm_miscellaneous_information.pdf

Table of Contents

1. Synthesis and characterization

The compounds $(PPh_4)_2[ReF_6]\cdot 2H_2O$ and $(PPh_4)_2[OsF_6]\cdot 2H_2O$ were prepared as previously described,[1] and dried at 100°C under vacuum on a Schlenk line to obtain desolvated precursors, $(PPh_4)_2[MF_6]$. Dichloromethane (containing less than 40 ppm of water) was purified using an Innovative Technologies solvent purification system. All other reagents and solvents were commercially available and used as received without further purification.

Synthesis of ***1***. The synthesis was performed under a dry argon atmosphere using standard Schlenk or glovebox techniques. $(CH_3)_3SiCN$ (0.1 mL, 0.8 mmol) was first added to a solution of $(PPh_4)_2[ReF_6]$ (196 mg, 0.20 mmol) in dichloromethane (110 mL). After stirring for 3 hours, the solvent was removed using a dynamic vacuum. A mixture of dichloromethane (60 mL) and $(CH_3)_3SiCN$ (0.1 mL, 0.8 mmol) was then added to the resulting brown solid, which dissolves. The mixture was left stirring overnight. It is worth mentioning that this two-steps reaction is working in similar manner when using less dichloromethane (12 mL in each step) leading to a $(PPh_4)_2[ReF_6]$ suspension rather than a solution. After a few hours, a light brown solution is systematically obtained.
After removal of the solvent using a dynamic vacuum, *N*,*N*-dimethylacetamide (2 mL; containing around 2000 ppm of water) was added to dissolve the residue, and the solution was filtered with a VWR syringe filter (25 mm, 0.2 mm PTFE). Slow addition of diethylether (50 mL; containing around 200 ppm of water) to the filtrate afforded $(PPh_4)_2[trans\text{-}ReF_4(CN)_2]\bullet H_2O$ in a yield of >80%. The water molecule observed in the crystal structure most likely originates from the solvents. It is worth mentioning that a stoichiometric amount of $(CH_3)_3SiCN$ (2 equivalents) leads to a mixture of species, $[MF_{6-n}(CN)_n]^{2-}$ ($n \leq 2$), while an excess of 8 up to 10 equivalents (in total for the two-step reaction) does not change the final bis-substituted product.
Crystallization of ***1***. Single crystals suitable for X-ray crystal structure determination were obtained by slow vapor diffusion of diethylether into a *N*,*N*-dimethylacetamide solution of $(PPh_4)_2[trans\text{-}ReF_4(CN)_2]$ in air.. Elemental analysis: calcd (%) for $C_{50}H_{42}F_4N_2OP_2Re$: C 59.40, H 4.19, N 2.77, F 7.52; found: C 59.17, H 4.10, N 3.29, F 6.76. IR of **1** (solid, $\bar{\nu}$/cm^{-1}) 615 (m), 689 (vs), 719 (vs), 762 (vs), 856 (w), 996 (s), 1104 (vs), 1165 (w), 1190 (m), 1317 (m), 1436 (s), 1484 (m), 1585 (m), 1619 (m), 2128 (m), 3025 (w), 3064 (w), 3082 (w), 3484 (m), 3511 (m), 3557 (m).

Synthesis and crystallization of ***2***. The synthetic procedure and crystallization employed for **2** are identical to that of **1**, but $(PPh_4)_2[ReF_6]$ was replaced by $(PPh_4)_2[OsF_6]$. Yield: ~60%. Elemental analysis: calcd (%) for $C_{50}H_{42}F_4N_2OP_2Os$: C 59.16, H 4.17, N 2.76, F 7.49; found: C 58.73, H 4.24, N 2.72, F 7.34. IR of **2** (solid, $\bar{\nu}$/cm^{-1}) 561 (vs), 615 (m), 689 (vs), 719 (vs), 762 (s), 856 (w), 996 (s), 1105 (vs), 1165 (w), 1190 (m), 1317 (m), 1436 (s), 1484 (m), 1585 (m), 1617 (m), 2124 (m), 3025 (w), 3065 (w), 3083 (w), 3476 (m), 3510 (m), 3551 (m).

2. Crystallographic Data

Diffraction intensities were collected on a Bruker APEXII Quasar diffractometer with Mo K_α radiation (λ = 0.71073 Å) for **1** and **2** at 120 K and 122 K, respectively. The structures were solved by direct methods, and all non-hydrogen atoms were refined anisotropically by least-squares on F^2 using the SHELXTL program. Anisotropic thermal parameters were assigned to all non-hydrogen atoms. Hydrogen atoms on organic ligands were generated by the riding model.[2] CCDC 1531669 (**1**) and 1531670 (**2**), contain the supplementary crystallographic data for this paper. These data can be obtained free of charge from The Cambridge Crystallographic Data Centre via https://www.ccdc.cam.ac.uk/structures/.

Table S1. Crystallographic Data and Structural Refinements for **1** and **2**.

Compound	**1**	**2**
Molecular formula	$C_{50}H_{42}F_4N_2OP_2Re$	$C_{50}H_{42}F_4N_2OP_2Os$
Formula weight	1010.99	1014.99
Crystal system	Triclinic	Triclinic
Space group	*P*-1	*P*-1
a / Å	9.7647(3)	9.7533(5)
b / Å	10.5251(3)	10.5287(5)
c / Å	11.5912(3)	11.5390(5)
α / °	75.5692(8)	75.641(2)
β / °	70.3354(10)	70.417(2)
γ / °	77.4645(9)	77.539(2)
V / Å^3	1074.76(5)	1070.04(9)
Z	1	1
ρ_{calcd} / g cm^{-3}	1.562	1.575
μ(*Mo K*$_\alpha$) / mm^{-1}	2.959	3.112
F000	505	506
θ range / °	1.901-27.531	2.789-27.878
collected reflns	13734	24661
unique reflns	4910	5078
reflns [$I \geq 2\sigma(I)$]	4907	5050
params / *restraints*	277/0	277/0
max / *min* $\Delta\rho_r$ / e Å^{-3}	0.770/-0.445	0.879/-0.340
GOF	1.088	1.102
R_1 [$I \geq 2\sigma(I)$][(a)]	0.0159	0.0212
wR_2(all data)[(b)]	0.0384	0.0489

[(a)] $R_1 = \sum||F_o|-|F_c||/\sum|F_o|$, [(b)] $wR_2 = [\sum w(F_o^2-F_c^2)^2/\sum w(F_o^2)^2]^{1/2}$

Table S2. Selected bond lengths [Å] and bond angles [°] for **1** and **2**.

1		**2**	
Re1—F1	1.9359(10)	Os1—F1	1.9258(13)
Re1—F2	1.9507(10)	Os1—F2	1.9370(13)
Re1—C1	2.1347(19)	Os1—C1	2.115(3)
F1—Re1—F2	88.79(4)	F1—Os1—F2	89.38(6)
F1—Re1—C1	90.37(6)	F1—Os1—C1	90.35(7)
F2—Re1—C1	88.94(6)	F2—Os1—C1	88.85(7)

3. Infrared Spectroscopy

The IR spectra of crystalline solids were measured on a Nicolet 6700 FT-IR at room temperature.

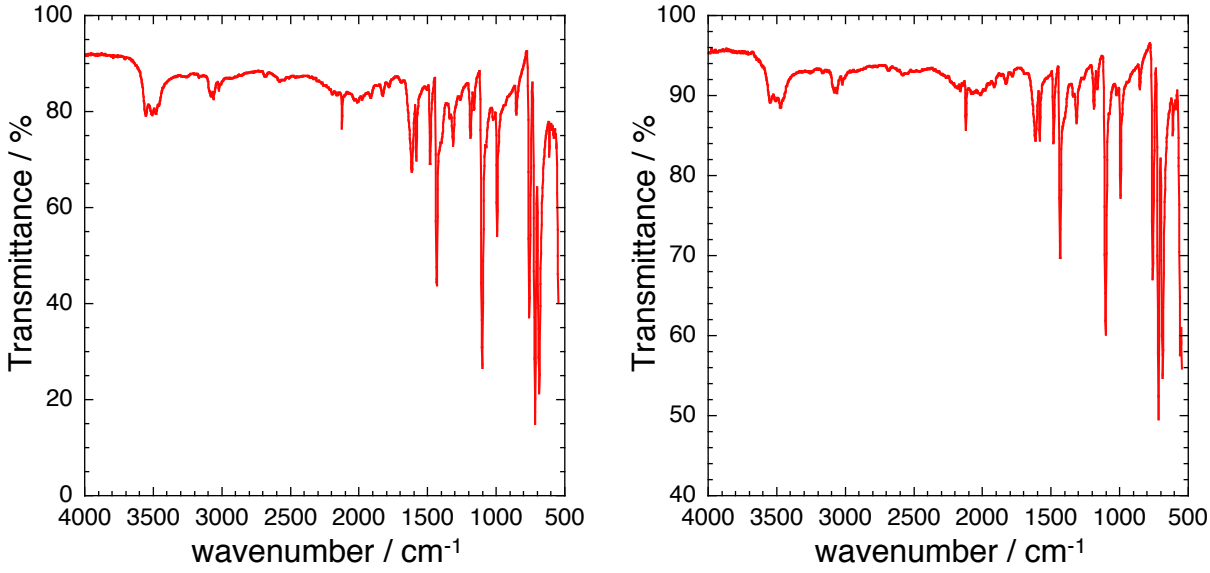

Figure S1. Room-temperature IR spectrum for **1** (*left*) and **2** (*right*) with $\bar{\nu}_{CN}$ = 2128 and 2124 cm^{-1} respectively.

4. Mass Spectrometry

ESI-MS was measured on a Thermo Scientific LCQ Fleet ion trap mass spectrometer.

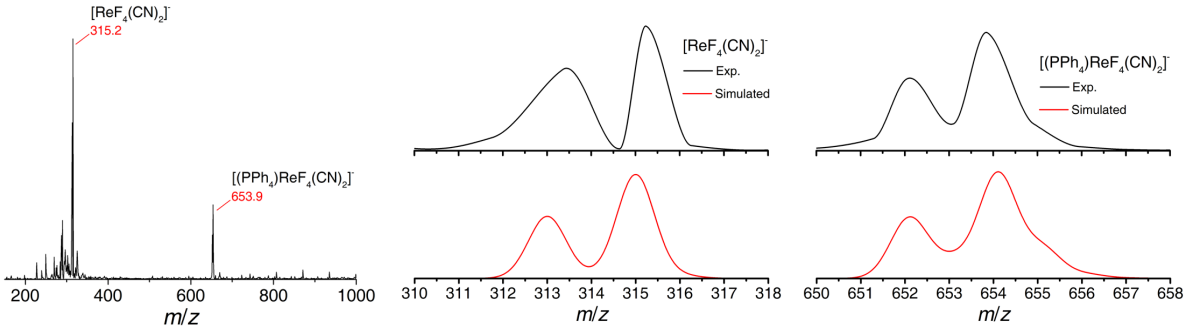

Figure S2. Mass spectrum (negative ion detection) for **1** (experimental pattern, black; simulated isotope pattern, red).

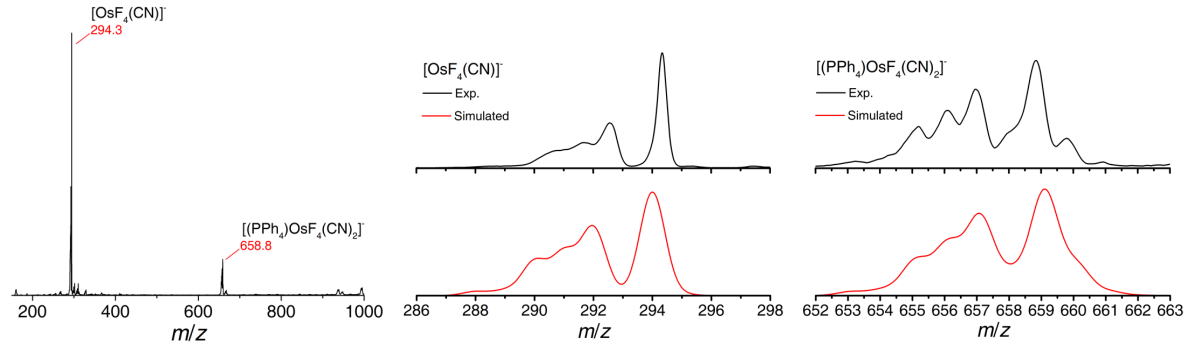

Figure S3. Mass spectrum (negative ion detection) for **2** (experimental pattern, black; simulated isotope pattern, red).

5. EPR Measurements

EPR spectra were collected on samples consisting of a microcrystalline powder suspended and frozen in mineral oil. This was done to prevent torqueing of the sample in applied fields. The transmission-type spectrometer used in this study employed a 17 T superconducting magnet in conjunction with a phase locked Virginia Diodes source combined with a series of frequency multipliers.[3] Detection of the field modulated signal was provided by an InSb hot-electron bolometer (QMC Ltd., Cardiff, U.K.). Temperature control was accomplished using an Oxford Instruments (Oxford, U.K.) continuous-flow cryostat.

6. Additional magnetic Data

Magnetic susceptibility measurements were performed on a Quantum Design SQUID MPMS-XL magnetometer and PPMS-II susceptometer housed at the Centre de Recherche Paul Pascal at temperatures between 1.8 and 400 K and *dc* magnetic fields ranging from -9 to +9 T. The *ac* magnetic susceptibility measurements were performed in an oscillating *ac* field of 1 to 6 Oe with frequencies between 10 and 10000 Hz and various *dc* fields (including zero). The measurements were carried out on polycrystalline samples (13.44, 23.10 for **1**, and 18.94 mg for **2**) suspended in mineral oil (typically 5-15 mg) and introduced in a sealed polyethylene bag (3 × 0.5 × 0.02 cm; typically, 27-30 mg). Prior to the experiments, the field-dependent magnetization was measured at 100 K on each sample in order to detect the presence of any bulk ferromagnetic impurities. In fact, paramagnetic or diamagnetic materials should exhibit a perfectly linear dependence of the magnetization that extrapolates to zero at zero *dc* field; the samples appeared to be free of any ferromagnetic impurities. The magnetic susceptibilities were corrected for the sample holder, the mineral oil and the intrinsic diamagnetic contributions.

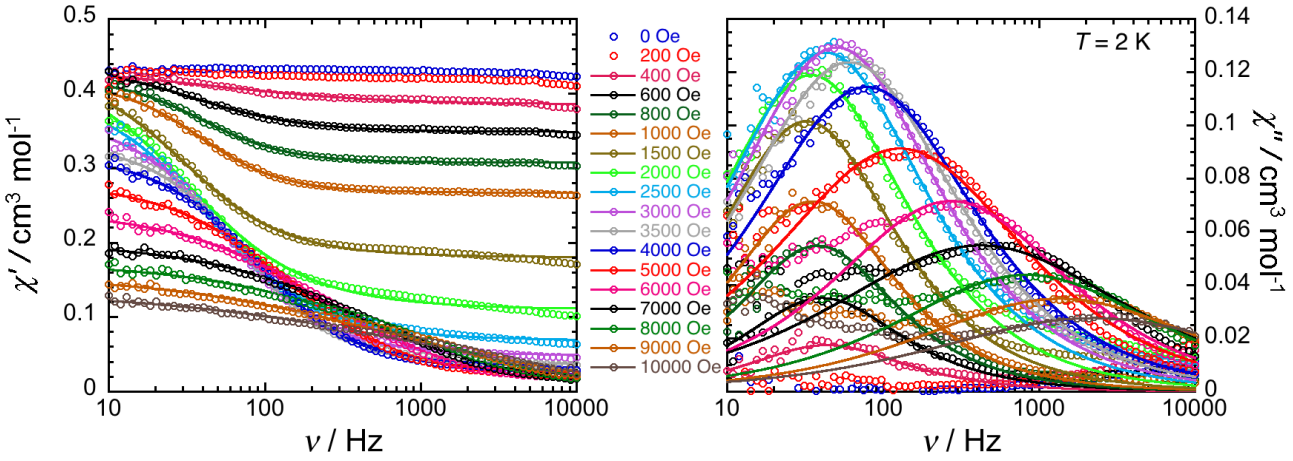

Figure S4. Frequency dependence of the real (χ', left) and imaginary (χ'', right) parts of the ac susceptibility for **1** collected at 2 K and varying dc fields. Solid lines are the best fits obtained with the generalized Debye model.

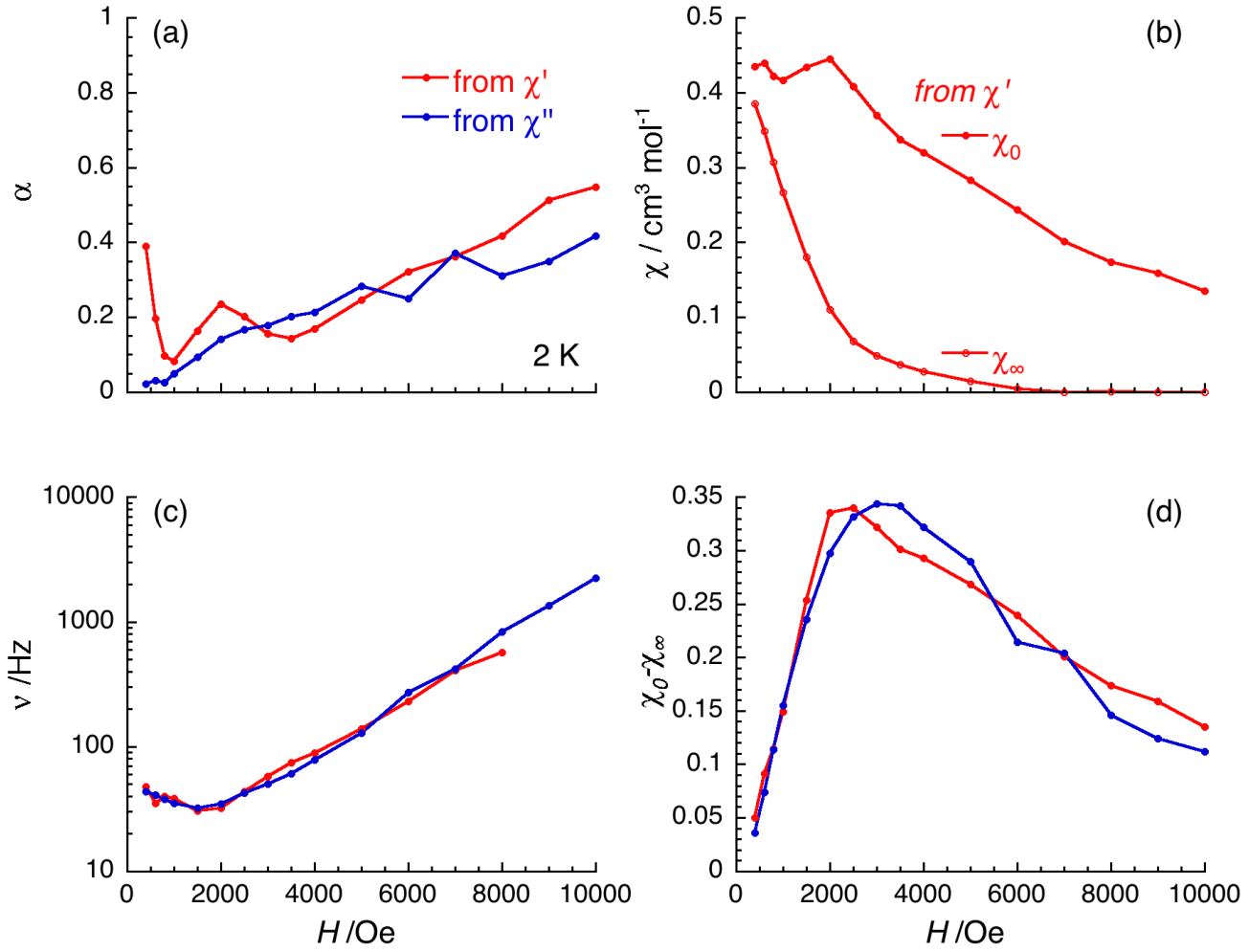

Figure S5. Field dependence of the parameters, α (a), ν (b), χ_0 & χ_∞ (c) and χ_0-χ_∞ (d) between 0 and 1 T deduced from the generalized Debye fit of the frequency dependence of the real (χ') and imaginary (χ'') components of the ac susceptibility at 2 K, shown in Figure S4 for **1**.

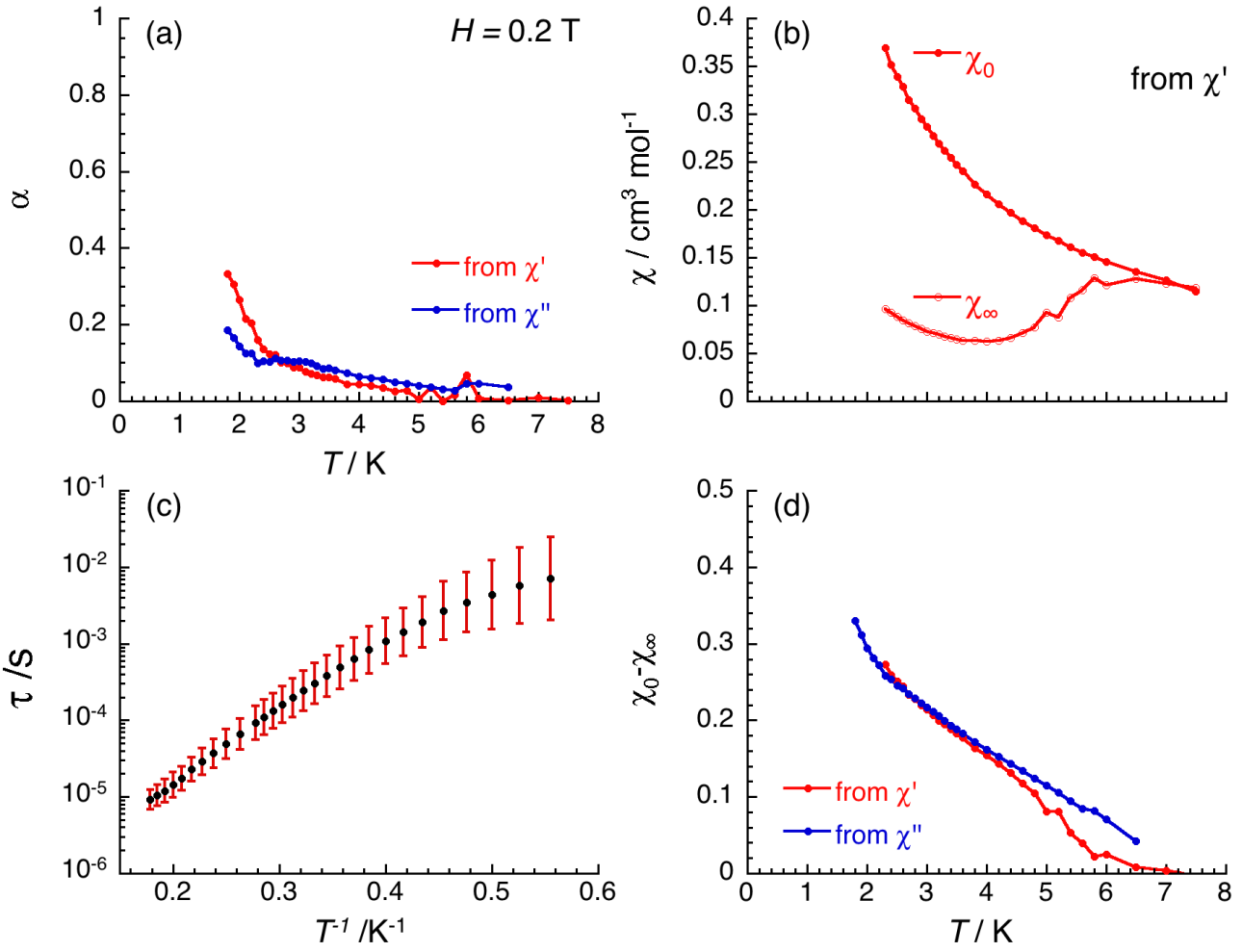

Figure S6. Temperature dependence of the parameters, α (a), χ_0 & χ_∞ (b), τ (c) and χ_0-χ_∞ (d) between 1.85 and 8 K deduced from the generalized Debye fit of the frequency dependence of the real (χ') and imaginary (χ'') components of the ac susceptibility at 0.2 T, shown in Figure 4 of the main text for **1**. On the bottom left figure, the temperature dependence of the relaxation time of **1** is shown at 0.2 T between 1.8 and 5.4 K (treatment of χ' *versus* ν and χ'' *versus* ν curves give undistinguishable results; both sets of data were averaged and plotted). The estimated standard deviations of the relaxation time (vertical solid bars) have been calculated from the α parameters of the generalized Debye fit (Figure 4) and the log-normal distribution as described in reference 4. The solid lines are guides for the eye.

7. Correlations between Real and Effective *g*-Tensors

For an $S = {}^3/_2$ system, which is the case of the complex **1**, the spin Hamiltonian can be written as follows:

$$\hat{H} = D\left(\hat{S}_z{}^2 - \tfrac{1}{3}S(S+1)\right) + E\left(\hat{S}_x{}^2 - \hat{S}_y{}^2\right) + \mu_B(g_x\hat{S}_xH_x + g_y\hat{S}_yH_y + g_z\hat{S}_zH_z)$$

The correlations between real and effective *g*-tensors are as follows:[5]

1) $D > 0$:

$$g_{x,eff} = g_x\left|\left(1 + \frac{1-3\gamma}{\sqrt{1+3\gamma^2}}\right)\right|; g_{y,eff} = g_y\left|\left(1 + \frac{1+3\gamma}{\sqrt{1+3\gamma^2}}\right)\right|; g_{z,eff} = g_z\left|\left(1 - \frac{2}{\sqrt{1+3\gamma^2}}\right)\right|$$

2) $D < 0$:

$$g_{x,eff} = g_x\left|\left(1 - \frac{1-3\gamma}{\sqrt{1+3\gamma^2}}\right)\right|; g_{y,eff} = g_y\left|\left(1 - \frac{1+3\gamma}{\sqrt{1+3\gamma^2}}\right)\right|; g_{z,eff} = g_z\left|\left(1 + \frac{2}{\sqrt{1+3\gamma^2}}\right)\right|$$

where $\gamma = E/D$.

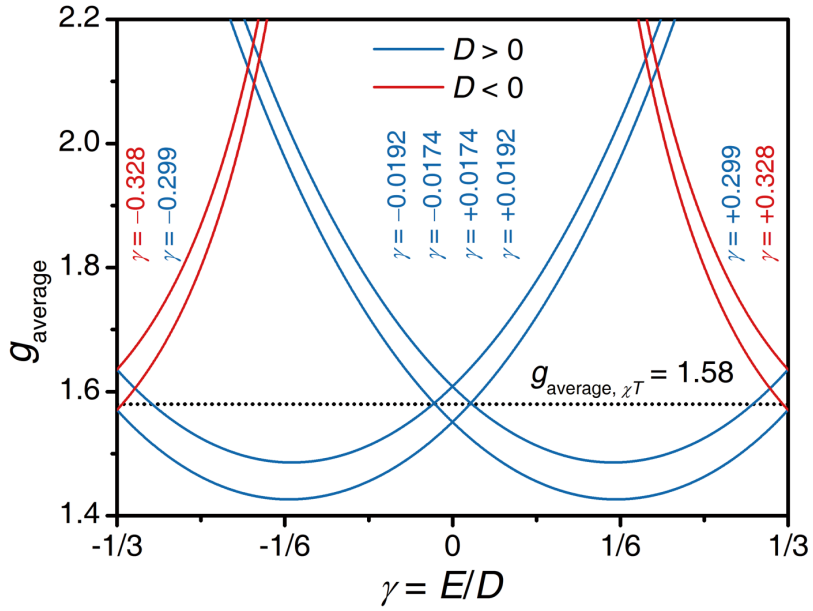

Figure S7. The plot of the calculated average *g*-factor ($g_{average}$) as function of the $\gamma = E/D$ value. According to the correlations between the real and the effective *g*-tensors mentioned above, the solid lines correspond to the possible scenarios in consideration of the effective *g*-tensors extracted from powder EPR for **1**, where $g_{average} = [(g_x^2 + g_y^2 + g_z^2)/3]^{1/2}$. The dashed line corresponds to the average *g*-factor (1.58) obtained from the experimental χT value (1.18 $cm^3\ mol^{-1}\ K$) at 270 K. The eight intersections of solid lines and the dashed line (in the range $-1/3 < \gamma < 1/3$) are the possible solutions, which are simultaneously in perfect agreement with both EPR and magnetic susceptibility (Table S3).

Table S3. Some possible $\gamma = E/D$ value and g-tensors from Figure S7.

No.	$\gamma = E/D$	D sign	E sign	g_x	g_y	g_z	$g_{average}$	Note
1	**−0.328**	**−**	**+**	**1.59**	**1.45**	**1.69**	**1.58**	**Most probable set of parameters.**
2	−0.299	+	−	1.73	1.05	1.84	1.58	1) g_y is unphysically small 2) the g-tensor is too anisotropic
3	−0.0192	+	−	2.26	0.59	1.43	1.58	1) g_x is unphysically large 2) g_y is unphysically small 3) the g-tensor is too anisotropic
4	−0.0174	+	−	0.70	2.38	1.15	1.58	1) g_x is unphysically small 2) g_y is unphysically large 3) the g-tensor is too anisotropic
5	+0.0174	+	+	2.38	0.70	1.15	1.58	Physically identical to set No.4: Permutation of the x and y axes and change of E sign.
6	+0.0192	+	+	0.59	2.26	1.43	1.58	Physically identical to set No.3: Permutation of the x and y axes and change of E sign.
7	+0.299	+	+	1.05	1.73	1.84	1.58	Physically identical to set No.2: Permutation of the x and y axes and change of E sign.
8	**+0.328**	**−**	**−**	**1.45**	**1.59**	**1.69**	**1.58**	**Physically identical to set No.1: Permutation of the x and y axes and change of E sign.**

8. CASSCF/NEVPT2 Calculations

All calculations were performed using the ORCA v4.0 program package.[6] The unoptimized crystal structure was used as the input geometry. The SA-CASSCF calculations were performed using the all-electron def2-TZVP basis set for carbon, nitrogen, and fluorine, while the SARC-TZVP basis set was used for rhenium.[7,8] Scalar relativistic effects were accounted for with the second-order Douglas-Kroll-Hess (DKH) procedure. To speed up the calculation the resolution of identity approximation was employed.[9] The auxiliary basis sets were generated using the 'autoaux' command as implemented in ORCA4.0.[10] The active space was defined to include the three 5*d*-electrons and the five 5*d*-orbitals (CAS(3,5)). All 10 quartet and all 40 doublet states were calculated. To account for dynamic correlations N-electron valence perturbation theory to the second order (NEVPT2) was performed on the converged CASSCF wavefunction. Spin−orbit coupling was treated using the mean field approximation as implemented in ORCA.[11] The results of these calculations are summarized in Figure S8 and Tables S4 and S5.

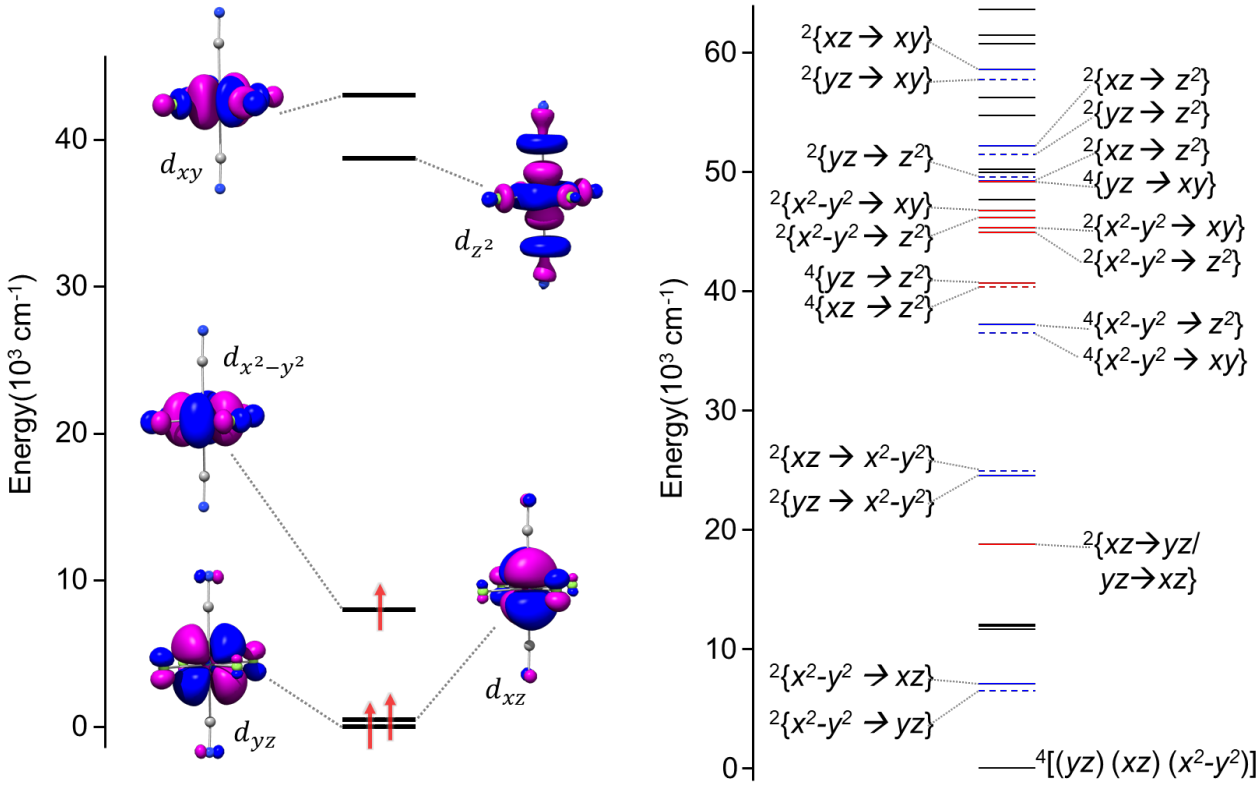

Figure S8. (Left) Qualitative MO diagram resulting from a SA-CASSCF/NEVPT2 calculation depicting the dominant configuration of the ground state. (Right) Energies of the 10 quartet 40 doublet states where the labels correspond to the excitation that best describes the main configuration of the excited state. Only states which contribute > 1 cm^{-1} to *D* are labelled. The ground state is labelled with the dominant configuration. The lines representing the energies of the excited states are coloured according to their contribution to *D*: red (positive), blue (negative) and negligible/zero (black). Furthermore, red/blue coloured states with dashed lines make negative contributions to *E*, while those depicted with solid lines make positive contributions. The numerical values for these contributions are shown in Table S4.

Table S4. Contributions^* to *D* and *E* for the excitations indicated in Figure S8.

Mult.	Transition	Energy (cm^{-1})	*D* (cm^{-1})	*E* (cm^{-1})
4	[(*yz*) (*xz*) (x^2-y^2)]	0	0	0
2	{x^2-y^2 → *yz*}	6497	-82.66	-76.96
2	{x^2-y^2 → *xz*}	7058	-67.58	62.07
2	{*xz*→*yz*}/{*yz*→*xz*}	18744	216.49	0.69
2	{*yz* → x^2-y^2}	24534	-67.58	9.20
2	{*xz* → x^2-y^2}	24939	-64.30	-15.04
4	{x^2-y^2 → *xy*}	36495	-153.92	-0.34
4	{x^2-y^2 → z^2}	37157	-2.41	0.07
4	{*xz* → z^2}	40313	58.16	-46.96
4	{*yz* → z^2}	40615	55.61	44.90
2	{x^2-y^2 → z^2}	44906	8.98	0.02
2	{x^2-y^2 → *xy*}	45259	5.39	0.01
2	{x^2-y^2 → z^2}	46139	2.31	0.01
2	{x^2-y^2 → *xy*}	46757	82.18	0.17
4	{*yz* → *xy*}	49189	2.47	0.42
2	{*xz* → z^2}	49202	-30.84	30.16
2	{*yz* → z^2}	49557	-29.54	-27.62
2	{*yz* → z^2}	51406	-4.06	-3.42
2	{*xz* → z^2}	52122	-7.63	4.05
2	{*yz* → *xy*}	57667	-2.26	-0.72
2	{*xz* → *xy*}	58503	-1.12	0.54
	Total		-80.21	-20.05 ($^E/_D$ = 0.25)

^Only states with contributions larger than 1 cm^{-1} are shown. * These contributions are calculated by second order perturbation theory. They do not add up to the total due to the neglect of numerous states with small contributions. While we have chosen this method for examining the individual contributions to *D,* we note that the effective Hamiltonian approach is the method used for the quoted value of *D* in the main text.

Table S5. Calculated zero-field splitting parameters.

	2PT*		Effective^	
	D (cm^{-1})	*E/D*	*D* (cm^{-1})	*E/D*
CASSCF	-56.7	0.24	27.4	0.30
NEVPT2	-80.2	0.25	-63.2	0.21

**D* is calculated using second order perturbation theory (2PT).
^*D* is calculated using an effective Hamiltonian.

9. X-ray spectroscopy

The rhenium $L_{2,3}$ X-ray absorption (XAS) and X-ray magnetic circular dichroism (XMCD) spectra of **1** were recorded at the ID12 beamline at ESRF – The European Synchrotron, Grenoble, France, using total fluorescence yield detection and in magnetic fields up to ±17 T. As the source of circularly polarized X-rays, we used the second harmonic of the emission from a helical undulator of APPLE-II type. The XMCD spectra were obtained as the direct difference between two consecutive XAS spectra recorded with right and left circularly polarized photons, using both magnetic field directions to ensure the absence of experimental artefacts. The isotropic XAS spectra were normalized to zero before the absorption edge and to unity far above the edge. The energy positions of the step functions relating the transitions into the continuum were defined as previously described.[1b] The integral of the white line at the L_2 edge was divided by two due to the occupation ratios of $2p_{3/2}$ and $2p_{1/2}$ core states. Since the magneto-optical sum rules are derived for line intensities $I(\hbar\omega)$ ($\hbar\omega$ is the photon energy) and not for the absorption cross sections, $\mu(\hbar\omega)$, an additional correction was utilized according to $I(\hbar\omega) = 1/(4\pi^2\alpha\,\hbar\omega) \times \mu(\hbar\omega)$. The integral of the isotropic XAS spectra are related to the $\langle\Sigma_i \mathbf{l}_i \cdot \mathbf{s}_i\rangle$ expectation value, summed over all 5d electrons, through the spin-orbit sum rule, which amounts to –1.56 in **1**.[12] It is worth mentioning that this value is very close to the one (–1.6) determined for the isoelectronic $[Os^{V}F_6]^{2-}$.[1b] The $\langle\Sigma_i \mathbf{l}_i \cdot \mathbf{s}_i\rangle$ expectation value depends on the electron distribution over the spin-orbit split 5d states, $5d_{3/2}$ and $5d_{5/2}$, and can be expressed in the electron occupation numbers $\langle\Sigma_i \mathbf{l}_i \cdot \mathbf{s}_i\rangle/\hbar^2 = -3/2 n_e^{3/2} + n_e^{5/2}$, where $n_e^{3/2} + n_e^{5/2} = n_e$ is the number of electrons in the 5d level. Given the strongly ionic nature of the complex, n_e was approximated to 3 leading to 1.82 and 1.18 for $n_e^{3/2}$ and $n_e^{5/2}$, respectively. An identical procedure was used for the normalization of the corresponding XMCD integrals to deduce spin and orbital moments:[12]

$$\langle L_z \rangle = -\frac{2\,n_h}{3} \times \frac{I_{L_3}^{XMCD} + I_{L_2}^{XMCD}}{I_{L_3}^{XAS} + I_{L_2}^{XAS}}$$

$$\langle S_{eff} \rangle = -\,n_h \times \frac{I_{L_3}^{XMCD} - 2 \times I_{L_2}^{XMCD}}{I_{L_3}^{XAS} + I_{L_2}^{XAS}}$$

where $\langle S_{eff}\rangle = \langle S_z\rangle + 7/2\,\langle T_z\rangle$ and $n_h = 10 - n_e$ is the number of holes in the 5d level. From these expressions the effective spin and orbital moments are calculated as $M_{spin,eff} = -2\langle S_{eff}\rangle$ and $M_{orbital} = -\langle L_z\rangle$ to yield $M_{spin,eff} = 1.1\ \mu_B$ and $M_{orbital} = 0.01\ \mu_B$. As the total moment was estimated at 1.6 μ_B (Figure 3, inset), the M_{spin} can be evaluated as $M_{total} - M_{orbital} = 1.6\ \mu_B$. This result allows an estimation of the dipole magnetic moment, $\langle T_z\rangle = (M_{spin} - M_{spin,eff})/7 = 0.07\ \mu_B$. Notably, this value is significantly larger than the vanishing value found for the isoelectronic $[Os^{V}F_6]^{2-}$ complex, which may be related to the symmetry lowering in *trans*-$[Re(CN)_2F_4]^{2-}$ as compared to the nearly perfectly octahedral OsF_6^-.[1b]

10. References

[1] (a) K. S. Pedersen, M. Sigrist, M. A. Sørensen, A.-L. Barra, T. Weyhermüller, S. Piligkos, C. Aa. Thuesen, M. G. Vinum, H. Mutka, H. Weihe, R. Clérac, J. Bendix, *Angew. Chem. Int. Ed.* **2014**, *53*, 1351; (b) K. S. Pedersen, D. N. Woodruff, S. K. Singh, A. Tressaud, E. Durand, M. Atanasov, P. Perlepe, K. Ollefs, F. Wilhelm, C. Mathonière, F. Neese, A. Rogalev, J. Bendix, R. Clérac, *Chem. Eur. J.* **2017**, *23*, 11244.

[2] (a) G. M. Sheldrick, *Acta Crystallogr. A*, **2008**, *64*, 112; (b) G. M. Sheldrick, *SHELXTL 6.10*, Bruker Analytical Instrumentation, Madison, Wisconsin, USA, **2000**.

[3] A. Hassan, L. Pardi, J. Krzystek, A. Sienkiewicz, P. Goy, M. Rohrer, L.-C. Brunel, *J. Magn. Reson.* **2000**, *142*, 300.

[4] D. Reta, N. F. Chilton, *Phys. Chem. Chem. Phys.* **2019**, *21*, 23567-23575.

[5] (a) T. Yamane, K. Sugisaki, H. Matsuoka, K. Sato, K. Toyota, D. Shiomi, T. Takui, *Dalton Trans.* **2018**, *47*, 16429; (b) T. Yamane, K. Sugisaki, T. Nakagawa, H. Matsuoka, T. Nishio, S. Kiniyo, N. Mori, S. Yokoyama, C. Kawashima, N. Yokokura, K. Sato, Y. Kanzaki, D. Shiomi, K. Toyota, D. H. Dolphin, W.-C. Lin, C. A. McDowell, M. Tadokoro, T. Takui, *Phys. Chem. Chem. Phys.* **2017**, *19*, 24769.

[6] F. Neese, *Wiley Interdiscip. Rev. Comput. Mol. Sci.* **2018**, *8*, e1327.

[7] F. Weigend, R. Ahlrichs, *Phys. Chem. Chem. Phys.* **2005**, *7*, 3297.

[8] D. A. Pantazis, X. Y. Chen, C. R. Landis, F. Neese, *J. Chem. Theory Comput.* **2008**, *4*, 908.

[9] F. Neese, *J. Comput. Chem.* **2003**, *24*, 1740.

[10] G. L. Stoychev, A. A. Auer, F. Neese, *J. Chem. Theory Comput.* **2017**, *13*, 554.

[11] B. A. Heß, C. M. Marian, U. Wahlgren, O. Gropen, *Chem. Phys. Lett.* **1996**, *251*, 365.

[12] B. T. Thole, P. Carra, G. van der Laan, *Phys. Rev. Lett.* **1992**, 68, 1943.